Journal of Materials Chemistry A

High efficiency hysteresis-less inverted planar heterojunction perovskite solar cell with NiOx hole contact layer

Journal:	*Journal of Materials Chemistry A*
Manuscript ID	TA-ART-10-2015-008193.R1
Article Type:	Paper
Date Submitted by the Author:	06-Nov-2015

Complete List of Authors:	Yin, Xingtian; Xi'an Jiaotong University, Electronic Materials Research Laboratory, School of Electronic and Information Engineering Que, Meidan; Xi'an Jiaotong University Xing, Yonglei; Xi'an Jiaotong University, Electronic Materials Research Laboratory, School of Electronic and Information Engineering Que, Wenxiu; Xi'an Jiaotong University, Electronic Materials Research Laboratory, School of Electronic and Information Engineering

High efficiency hysteresis-less inverted planar heterojunction perovskite solar cell with NiO_x hole contact layer

Xingtian Yin, Meidan Que, Yonglei Xing, Wenxiu Que**

Electronic Materials Research Laboratory, International Center for Dielectric Research, Key Laboratory of the Ministry of Education, School of Electronic & Information Engineering, Xi'an Jiaotong University, Xi'an 710049, Shaanxi, People's Republic of China

Abstract

Hysteresis-less inverted planar heterojunction perovskite solar cell with 14.42% power conversion efficiency (PCE) was successfully fabricated by employing solution-derived NiO_x film as the hole selective contact. Here, the non-stoichiometric transparent NiO_x film is composed of a lot of small NiO_x nanocrystals with a cubic crystal structure. Inverted planar heterojunction perovskite solar cells based on the as-prepared NiO_x hole selective contacts show a much higher PCE and air storage stability than the control device fabricated from the PEDOT: PSS film as the hole selective contact, since the NiO_x has a better electron blocking property due to its high conduction band edge position. The thickness of the NiO_x contact strongly influences the performance of the NiO_x-based perovskite solar cells, which include the PCE, hysteresis behaviors and air storage stability due to the thickness-dependent morphology of the NiO_x contact.

Keywords: NiO_x, hole selective contact, planar heterojunction perovskite solar cell, hysteresis, stability

* Corresponding author:
Email address: xt_yin@mail.xjtu.edu.cn; wxque@mail.xjtu.edu.cn
Tel.: +86-29-83395679; Fax: +86-29-83395679

1. Introduction

Organic-inorganic hybrid perovskite solar cells have achieved a rapid development during the past three years, and the overall power conversion efficiency (PCE) has recently exceeded 20% due to their excellent light harvesting, high charge carrier mobility and long carrier life time [1-4]. The reported perovskite solar cells can be mainly divided into two classes based on their structures. The first class evolves from solid state dye sensitized solar cells and contains a mesoporous film as the support layer of perovskite, for example, the TiO_2 and Al_2O_3 mesoporous films [5-7], while the other class is known as planar heterojunction solar cells which have a similar structure with the p-i-n silicon solar cells [8, 9].

In a typical planar heterojunction perovskite solar cell, perovskite absorption layer is sandwiched between a hole contact layer and an electron contact layer. Compact TiO_2 and ZnO films usually work as the electron contacts in the n-i-p type devices, and their efficient electron extraction ability has been demonstrated by many works [8-10]. While, 2,2′,7,7-tetrakis(N,N-di-4-methoxyphenylamino)-9,9′-spirobifluorene (spiro-OMeTAD) is the most frequently used as the hole contact in these devices. However, spiro-OMeTAD has an extremely high price and poor stability against temperature and moisture [11]. Besides, Poly-(3,4-ethylenedioxythiophene): poly (styrenesulfonic acid) (PEDOT: PSS) and phenyl-C61-butyric acid methylester (PCBM) are frequently employed as the hole contact and electron contact in the p-i-n type devices, respectively [12-16]. Such kinds of devices are known as inverted planar heterojunction solar cells, and a PCE as high as 18.1% has been reported for them recently [17]. Unfortunately, the research in organic photovoltaic and light emitting diode (LED) has already proved that PEDOT: PSS is not good for the device long term stability due to its high acidity and hygroscopicity [18]. Hence, many inorganic semiconductors, which include MoO_x, NiO_x, V_2O_3, WO_3, and so on [18-20], have been employed to replace the PEDOT: PSS. Particularly, NiO is a low price material with superior thermal and chemical stability which has also been demonstrated to be a good hole selective contact for perovskite solar cells due to its proper work function and high conduction band edge position that can transport holes and block electrons efficiently[21]. For example, NiO_x film and NiO_x nanoparticles were combined together to fabricate mesoscopic $NiO_x/CH_3NH_3PbI_3$ perovskite solar cells, thus, resulting in a PCE of 11.6% [22, 23]. Xiaobao Xu et.

al. reported a PCE as high as 14.9% for the perovskite device by using mesoporous TiO_2 and NiO_x layers as electron selective contact and hole selective contact, respectively [24]. Inverted planar heterojunction perovskite solar cells based on NiO_x hole selective contacts had been also studied by many groups, and the PCE of NiO_x-based perovskite solar cell has been improved dramatically to 17.3% recently [25]. However, the NiO_x films were deposited by the costly pulsed laser deposition (PLD) method, which is not suitable for large scale fabrication. Actually, the PCE for perovskite solar cells based on most solution derived NiO_x films fell into a wide range from 7.6% to 15.4% [26-29].

Although the research of the NiO_x-based perovskite solar cells has achieved adequate progress over the past two years, several important issues are still left to be solved. Firstly, the PCE of perovskite solar cells based on solution derived NiO_x films should be further improved since it is still much lower than that of the Spiro-OMeTAD-based devices. Secondly, the hysteresis behaviors, which have been observed in almost all kinds of perovskite solar cells, can dramatically affect the accurate measurement of the PCE. Therefore, many steps have been taken to eliminate the hysteresis behaviors in the perovskite solar cells with different hole contact layers [17, 30-33], however, there are not any detailed hysteresis studies have been reported for the NiO_x-based perovskite solar cells so far. Thirdly, the stability of the solar cells is always one of the most important issues for the research of perovskite solar cells since it was first reported in 2009 [34]. Although there are several works to mention the stability study for some kinds of perovskite solar cells, the stability study of the NiO_x-based perovskite solar cells is really rare [35]. Here we report a solution-derived NiO_x film with a high transmission which was employed as the hole selective contact for inverted planar heterojunction perovskite solar cells. Results indicate that the thickness of the NiO_x hole selective contact has an important influence on the device performance, including the PCE, hysteresis behaviors and air storage stability. Finally, a hysteresis-less device with a PCE of 14.42% was achieved on the as-prepared and un-doped NiO_x hole selective contact, which was as high as those for the best-in-class NiO_x-based perovskite solar cells.

2. Experimental

2.1 NiO_x *nanoparticles solution preparation.*

3.084 g Nickel (II) acetylacetonate and 1.262 gdiethanolamine were added in 30 ml ethanol

and the mixture was continuously stirred at 60 °C for 12 h to make a clear green solution. Then, the green solution was transferred into a Teflon-lined stainless steel autoclave of 50 mL capacity and kept in an oven which was previously set to 150 °C for 10 h. The autoclave was cooled to room temperature after the reaction and the resulted dark green solution was filtered and centrifuged at 2000 rpm for 3 min successively. Followed the upper clear green solution was collected and mixed with about 400 ml cyclohexane, which was then stirred for tens of minutes until a turbid solution was obtained. Finally, the turbid solution was centrifuged at 10000 rpm for 6 min and the precipitation was collected and dispersed again in some ethanol to make NiO_x nanoparticles solutions with different concentrations.

2.2 NiO_x film deposition.

The NiO_x film was deposited by a spin-coating process using the obtained NiO_x nanoparticles solution as a precursor. The whole spin-coating process was conducted in air at 3000 rpm for 30 s. The thickness of the NiO_x films was adjusted by varying the concentration of the NiO_x precursor. Thus, the wet film was baked at 150 °C for 10 min and then further annealed at 500 °C in air for 1 h again.

2.3 PEDOT:PSS film deposition.

PEDOT:PSS (Clevios, Al4083) was mixed with isopropanol by volume ratio of 1:2. The mixture was ultrasonicated for 10 min and filtered through polytetrafluoroethylene (TPFE) filter (0.45 μm) before use. The PEDOT: PSS film was also deposited by the spin-coating process at 3000 rpm for 60 s and then dried at 130 °C for 20 min.

2.4 Device fabrication.

To prepare the perovskite precursor solution, 2.3 g PbI_2 (Weihua-Solar) and 0.8 g CH_3NH_3I (Weihua-Solar) were dissolved in 1.5 mL dimethylsulphoxide (DMSO, Alfa-Aesar) and 3.5 ml N,N-dimethylformamide (DMF, Alfa-Aesar) solution at 70 °C with vigorous stirring for 12 h，and the resulted solution was then filtered through TPFE filter (0.45 μm) to make a clear yellow precursor. Patterned FTO substrates were fabricated by etching the FTO glass with the help of zinc powder and HCl. Followed the patterned substrates were cleaned by sonication in hot Helmanex solution, acetone, ethanol, and deionized water, successively. The NiO_x or PEDOT:PSS coated substrates were transferred into a glove box and the perovskite film layer was deposited on the top

of the NiO_x or PEDOT:PSS films by the spin-coating process, which includes a low speed of 1000 rpm for 5 s to spread the solution, and a high speed of 3000 rpm for 35 s to evaporate the solvent. At the end of the spin-coating, 0.13 ml chlorobenzene was dripped onto the film while spinning. Then the films were baked at 100 °C for 30 min. The PCBM (American Dye Sources) layer was deposited onto the perovskite film from a 20 mg/mL chlorobenzene solution at 1500 rpm for 45 s. Finally, an Ag film with a thickness of about 100 nm was deposited onto the PCBM layer by a thermal evaporation to finish the device fabrication.

2.5 Characterization.

Microstructural properties of the NiO_x nanoparticles were observed by a transmission electron microscopy (TEM, JEM-2010, JEOL Inc., Japan). Thermo gravimetric analysis (TGA) was conducted in air with a heating rate of 20 °C min^{-1} using a thermal analyzer (NETZSCH STA 449C, Germany). X-ray diffraction (XRD) analysis was employed to characterize the crystalline properties of the films from a D/max 2400 X Series X-ray diffractometer (Rigaku, Japan). Scanning electron microscopy (SEM, JSM-6390, JEOL Inc., Japan) and atomic force microscopy (AFM, Cypher S, Asylum Research) were used to observe the morphological properties of the films and devices. X-ray photoelectron spectroscopy (XPS, AXIS Ultrabld, Kratos) was used to analyze the element composition of the NiO_x film. The UV-Vis absorption spectra of the films were tested by a JASCO V-570 UV/VIS/NIR Spectrometer. The J-V curves of the as-fabricated devices were measured in air using a PVIV-201V I-V Station (Newport Oriel). The illumination source was calibrated by a Newport 91150V reference cell system. The dwell time for each scan point was changed from 10 ms (scanning rate 1000 mV/s) to 500 ms (scanning rate 20 mV/s) to investigate the hysteresis effects of the devices. All the device performance parameters were acquired with a scanning rate of 100 mV/s unless otherwise stated. The steady state power conversion efficiency was tested by keeping the device at maximum power point for 100s. The external quantum efficiency (EQE) spectra of the devices were tested in air without bias light by a Qtest Station 1000ADX system (Growntech. Inc). The chopper frequency was 180 and the step for monochrometer was 5 nm.

3. Results and discussion

Many solution-derived methods have been successfully used to deposit NiO_x films and the

optical-electronic properties of the resulted NiO_x films heavily depend on the employed methods. Here, we employed a hydrothermal method to prepare NiO_x nanoparticles precursor. Figure 1 shows the TEM images of the NiO_x precursor. It can be observed from Fig. 1 that the contrast is very low in the low magnification TEM image due to the small size and weak crystallinity of the NiO_x nanoparticles, but the NiO_x nanoparticles with a size of ~5 nm can be still seen from the HRTEM image as shown in the inset of Fig. 1. Actually, these NiO_x nanoparticles are buried in a lot of organic components, which can be destroyed by the electron beams after TEM characterization (as seen in Fig. S1). The existence of abundant organic components can also be proved by the TGA of the NiO_x powder obtained by drying the precursor at 150 °C for 20 min. As can be seen in Fig. S2, the powder lost about 10% of its original weight around 100 °C which can be attributed to the water takeup of the powder. As the temperature increased, the powder weight experienced a dramatic loss due to the decomposition and combustion of the organic components, especially in the region from 200 °C to 500 °C (more than 50% of its original weight).

Figure 2a shows the XRD patterns of FTO substrate and NiO_x film after being annealed at 500 °C in air for 1 h. As compared to the XRD pattern of FTO substrate, several additional peaks can be clearly observed at 37.2°, 43.3° and 62.9° for the NiO_x coated substrate, which can be assigned to the (111), (200) and (220) planes of cubic NiO_x crystal phase, indicating a good crystalline for the NiO_x film. To determine the optical band gap of the as-prepared NiO_x, we measured the absorption spectrum of the NiO_x film deposited on a quartz substrate and the result is shown in Fig. 2b, where $(ABS*h\upsilon)^2$ was plotted as a function of $h\upsilon$. The calculated band gap for the NiO_x film is 3.7 eV, which is in accordance with previous report [36]. The element composition of the NiO_x film was characterized by XPS analysis, and Fig. 2c shows the XPS spectra of Ni 2p core level. The peak at 860.8 eV is ascribed to the shake up process of NiO structure. While the peak at 853.6 eV should be ascribed to Ni^{2+}, indicating the existence of NiO. It should be mentioned here that a satisfactory fit obtained by adding only two peaks for Ni^{3+} at 855.0 eV and 856.2 eV on top of a Shirley back ground indicates the existence of Ni_2O_3 and NiOOH components [20]. Hence, the as-obtained film should be noted as NiO_x rather than NiO.

The NiO_x films with different thickness were deposited on FTO substrates by changing the concentration of the NiO nanoparticles precursors, and the morphological properties of the

resulted films were characterized by SEM and AFM. As shown in Fig. 3a, the surface morphology of bare FTO is like hills with a root mean square (RMS) roughness as high as 16.992 nm, which can be effectively decreased through depositing NiO_x film. As the thickness of the NiO_x film increases from 5 nm in Fig. 3b to 190 nm in Fig. 3f, the RMS roughness decreases from 10.400 nm to 2.025 nm. However, if the NiO_x film is too thin (Fig. 3b), it may be discontinuous, and thus the crystal morphology of FTO can be still seen clearly. As the thickness of the NiO_x film increases to 20 nm, the NiO_x film can complete a full coverage for the surface of FTO except for many cracks along the boundaries of FTO as seen in Fig. 3c. Actually, these cracks can be partially avoided by increasing the NiO_x film thickness to 55 nm as seen in Fig. 3d. When the thickness of the NiO_x film further increases up to 90 nm and 190 nm in Fig.s 3e and f, all the cracks disappear completely, and the FTO surface becomes very smooth and homogenous. It is interesting to note that all the NiO_x films shown in Fig. 3 are composed of small nanoparticles with a size of 10~30 nm, which might be aggregated from the NiO_x nanoparticles precursor during the annealing.

To fabricate the perovskite solar cells, we deposited $CH_3NH_3PbI_3$ perovskite films on the NiO_x coated substrate, and the top-view SEM image of the as-prepared perovskite film is shown in Fig. 4a. It can be seen that the perovskite film shows a full coverage on the NiO_x film and the perovskite film crystal sizes are in the range from 100 nm to 500 nm. The as-prepared perovskite film also has a good crystallinity (Fig. S3a) and efficient absorption in the visible region (Fig. S3b). Figure 4b shows a false color cross-sectional-view SEM image of a typical device with a structure of glass/FTO/NiO_x/$CH_3NH_3PbI_3$ film/PCBM/Ag. In this device structure, the thickness of the NiO_x film, which is composed of small nanoparticles, is about 90 nm. The perovskite film is pinhole free and has a thickness of 330 nm. A PCBM layer with about 80 nm was deposited on the top of the perovskite film, followed a layer of Ag film with a thickness of 100 nm as the cathode. Here, the NiO_x layer and PCBM layer work as the hole selective contact and electron selective contact, respectively, as shown in the schematic band diagram (Fig. 4c).

Figure 4d shows the J-V curves of the perovskite solar cells with different hole selective contacts, where the J-V curve for the device without any hole selective contact is also presented for comparison. Both the open circuit voltage (V_{oc}) and short circuit current density (J_{sc}) are very

low if the perovskite film is directly deposited on the FTO substrate, thus, resulting in a very poor device performance with a PCE of only 1.15%. However, even if 5 nm thick NiO_x film is deposited between the perovskite layer and FTO substrate, the PCE of the device increases to 8.39% rapidly due to a great improvement of V_{oc}, J_{sc} and fill factor (FF). As the thickness of the NiO_x film is further increased, the FF increases steadily to around 75.2%, while the J_{sc} reaches the highest value of 18.68 mA/cm^2 for the device with the NiO_x film thickness of 20 nm and then decreases gradually for the devices with thicker NiO_x film. The V_{oc} is able to maintain a high value of 1.09 V when the thickness of the NiO_x film is in the range between 55 nm and 90 nm. However, if the thickness of the NiO_x film is doubled to 190 nm, both the V_{oc} and J_{sc} decrease dramatically, and thus leading to a deterioration of device performance. Hence, the best device performance can be obtained when the thickness of the NiO_x film is 90 nm. Together with of a V_{oc} of 1.09 V, a J_{sc} of 17.93 mA/cm^2, and a FF of 73.8%, a highest PCE of 14.42% is thus achieved, which is as high as those for the best-in-class NiO_x-based perovskite solar cells as presented in Table S1. The steady state power conversion efficiency was also tested by keeping the device at maximum power point to ensure a reliable result. For a device with a J-V scanning PCE of 14.33%, the steady state power conversion efficiency was 14.18%, indicating a good consistency. The details about the steady state power conversion efficiency can be found in supporting information. As a comparison, the optimized PEDOT: PSS control device only output a V_{oc} of 0.93 V and a PCE of 11.63%, which are much lower than those of our best NiO_x devices. The great improvement for the NiO_x-based devices should be ascribed to their superior electron blocking ability due to the high conduction band edge position of the NiO_x (see Fig. 4c), which can be demonstrated by the better diode property as shown in Fig. S5. A detail summary of the device performance parameters is presented in table 1.

Figure 4e compares the EQE spectra of different devices. The J_{sc} for each device can be calculated by integrating the overlap of EQE and the AM 1.5G solar photon flux, and the obtained results are also listed in table 1. Obviously, the J_{sc} values calculated from the EQE spectra are roughly in accordance with those obtained from J-V curves. Figure 4f shows the transmission spectra of the PEDOT: PSS or the NiO_x film coated FTO substrates. Several interesting phenomena can be observed when we compare the EQE spectra and the transmission spectra.

Firstly, although the PEDOT: PSS film has a similar or even higher transparence as compared with the NiO_x film (20 nm and 55 nm), the PEDOT: PSS-based device shows a much lower EQE. Secondly, the transparence of the NiO_x film with 190 nm is only slightly smaller than that of the NiO_x film with 90 nm, however, the EQE of the device with 190 nm NiO_x film is much lower than that of the device with 90 nm NiO_x film. Above phenomena can be explained as follows: for one thing, the NiO_x film has a better electron blocking property due to its high conduction band edge position as shown in Fig. 3c, thus, leading to less electron recombination at the interface between the NiO_x film and the perovskite film. For another, since the NiO_x film is composed of many small NiO_x nanoparticles, thus, the thicker NiO_x film (190 nm) introduces much more crystal boundaries, which can be traps for the carriers, leading to more recombination in the NiO_x film and a decrease of J_{sc}.

Hysteresis behavior is an important issue for the perovskite solar cells, which has been observed and reported in many kinds of perovskite solar cells. Devices with hysteresis behaviors show a great discrepancy between the forward and reverse J-V scan, leading to an over estimation or under estimation for the real PCE. Therefore, more and more researchers have paid their attentions to this issue. Here, we investigated the hysteresis behaviors of our devices by changing the scanning rate and direction. Figures 5a and b show the J-V curves of the devices with different NiO_x film thicknesses, in which the subscript "reverse" means scanning from V_{oc} to J_{sc}, while the subscript "forward" means scanning from J_{sc} to V_{oc}. As shown in Fig. 5a, no matter how fast the scanning rate is, the device with the NiO_x film thickness of 20 nm shows a great discrepancy between the forward scanning and the reverse scanning. Although all these curves show a similar J_{sc}, the V_{oc} and FF values obtained from the forward scanning are much larger than those obtained from the reverse scanning, thus, resulting in an increase of PCE. Meanwhile, it is also noted that even if the scanning is in the same direction, the J-V curves still mismatch each other slightly as the scanning rate is changed, especially for the reverse scanning. However, when the thickness of the NiO_x film is increased to 90 nm, all the J-V curves overlap each other as shown in Fig. 5b, suggesting little hysteresis behavior can be observed. These results indicate that the hysteresis behavior of the as-fabricated devices depends on the thickness of the NiO_x film badly. In order to make this point clearly, we compared the performances of the devices fabricated from the NiO_x

films with different thicknesses, and the results are shown in Fig. 6. The x axis in each panel of Fig. 6 represents the devices with different hole selective contacts (including the PEDOT: PSS control device), while the y axis represents the difference of the performance parameters between the forward scanning and the reverse scanning. The scanning rate for both directions is 100 mV/s. The bigger the absolute value of the y axis is, the worse the hysteresis phenomenon is. Clearly, it can be seen that when the NiO_x film is thin (5 nm and 20 nm), the difference for V_{oc} between two scans is more than 100 mV, and the difference for FF is between 4%~10%. Together with a slight difference for J_{sc}, thus, the PCE shows a big difference in the range of 1.8~3.1%. However, as the thickness of the NiO_x film increases to above 55 nm, the V_{oc} values obtained from the two scans converge, and the differences for J_{sc} and FF between two scans decrease to around 0.05 mA/cm^2 and 1%, respectively. Therefore, the hysteresis-less J-V curves can be obtained for these NiO_x-based devices fabricated from the thicker NiO_x films, which are even better than the PEDOT: PSS control device.

The origin for the hysteresis behaviors of the perovskite solar cells has been investigated in many different device structures, and several possible reasons were proposed to explain this phenomenon, such as the defects in the perovskite crystal surface and boundaries [12], ion migration in perovskite layer [37, 38], ferroelectricity [39, 40], unbalanced electron flux and hole flux in carrier contacts [17], and so on. However, it is too far to make a conclusion for this issue at present, and primary reason for a certain device is also different from sample to sample, which should be determined by their structures and materials. In our case, the efficient hole extraction ability of the NiO_x selective contact and the high quality of the perovskite film should be the most important two reasons for the reduced hysteresis behaviors for our devices due to thick NiO_x contact. While the serious hysteresis behaviors for the devices with thinner NiO_x contact should be resulted from the direct contact between the perovskite film and FTO substrate due to the incomplete coverage or cracks of the NiO_x films as seen in Fig.s 3b, c and d. A more in-depth investigation for the hysteresis behaviors is still undertaken in our lab.

Furthermore, we studied the air storage stability of our devices by measuring the J-V curves of the devices after being exposed to ambient air for different duration. Figure 7 shows the changes of V_{oc}, J_{sc}, FF and PCE with the exposure time, respectively. It can be seen that the PCE

of the PEDOT: PSS-based device quickly deteriorates to ~20% of its original value in the first 24 h, which should be mainly attributed to the decrease of FF and J_{sc}. It is also interesting to note that the thickness of the NiO_x selective contact has a great influence on the device air storage stability. When the NiO_x contact layer is very thin (5 nm, 20 nm), both the V_{oc} and J_{sc} decrease slightly as the exposure time increases, but the FF decreases quickly in the first 48 h, resulting in a dramatic deterioration of the PCE. However, when the NiO_x contact layer is thick enough (55 nm and 90 nm), both the V_{oc} and J_{sc} can almost keep constant. Together with the gradually declined FF, the PEC still maintains more than 80% of its original value even after 150 h exposure. It should be mentioned here that the humidity of ambient air was between 45~56% during the entire measurement, and a detail record of the humidity is presented in Fig. S6. These results suggest that our NiO_x-based perovskite solar cells show a much better air storage stability than the PEDOT: PSS control device.

4. Conclusions

The NiO_x films with different thicknesses have been successfully deposited on FTO substrates by spin-coating the hydrothermal-derived NiO_x nanoparticles precursor. The as-prepared NiO_x films, which are composed of small nanoparticles with a size of 10~30 nm, have high transmission in the visible region with a band gap of 3.7 eV. Inverted planar heterojunction perovskite solar cell with the NiO_x film as hole contact shows a highest PCE of 14.42%, which is much higher than that of the PEDOT: PSS control device. Results indicate that the thickness of the NiO_x contact has a great effect on the PCE, hysteresis behavior, and air storage stability of the as-fabricated devices. A planar heterojunction perovskite solar cell with a hysteresis-less, high performance, and adequate air storage stability has been achieved from the NiO_x contact with 90 nm thick. The excellent performance of our NiO_x-based devices should be ascribed to the efficient hole extraction and electron blocking ability of the NiO_x contact as well as the high quality of the perovskite film. While the thickness dependent performance of our NiO_x-based device should be attributed to the different morphologies of the corresponding NiO_x films.

Acknowledgements

This work was funded by the National Natural Science Foundation of China under Grant No. 51502239, China Postdoctoral Science Foundation under grant 2015M582659, the Research Fund

for the Doctoral Program of Higher Education of China under grant 20120201130004, the Science and Technology Developing Project of Shaanxi Province under Grant No. 2015KW-001, partially by the National Natural Science Foundation of China Major Research Plan on Nanomanufacturing under Grant No. 91323303, and the 111 Project of China (B14040). The SEM work was done at International Center for Dielectric Research, Xi'an Jiaotong University, Xi'an, P. R. China.

Supporting Information

Supplementary data associated with this article can be found in the online version.

Table 1 Summary for the photovoltaic parameters of the devices with different hole selective contacts.

Hole selective contact	V_{oc} (V)	J_{sc} (mA/cm^2)		FF (%)	PCE (%)
		J-V	EQE		
no	0.58	8.41	-	23.5	1.15
PEDOT: PSS	0.93	17.11	16.66	73.2	11.65
5 nm NiO_x	1.00	16.23	15.61	51.6	8.39
20 nm NiO_x	1.05	18.68	18.03	64.8	12.71
55 nm NiO_x	1.09	18.07	18.32	69.6	13.71
90 nm NiO_x	1.09	17.93	17.77	73.8	14.42
110 nm NiO_x	1.07	15.92	15.73	73.7	12.55
190 nm NiO_x	0.98	12.73	13.08	75.2	9.38

Figure captions

Figure 1 TEM images of NiO_x nanoparticle precursor.

Figure 2 (a) XRD patterns of FTO substrate and NiO_x film; (b) Absorption coefficient as a function of photon energy for a NiO_x film on quartz substrate; (c) X-ray photoelectron spectra for Ni $2p_{3/2}$ core level of NiO_x film on FTO.

Figure 3 SEM and 3d-AFM images of (a) FTO substrate, (b) 5 nm NiO_x, (c) 20 nm NiO_x, (d) 55 nm NiO_x, (e) 90 nm NiO_x and (f) 190 nm NiO_x films on FTO substrate. Sizes of all 3d-AFM images are 1μm × 1μm.

Figure 4 (a) SEM images of $CH_3NH_3PbI_3$ film on NiO_x hole transport layer; (b) Cross-section view SEM image of a typical device with NiO_x hole transport layer; (c) Schematic band diagram of the perovskite solar cell; (d) J-V curves, (e) EQE spectra and (d) Transmission spectra for devices with PEDOT: PSS and NiO_x films as hole transport layers.

Figure 5 J-V curves obtained by scanning with different rates and direction. (a) device with 20 nm NiO_x; (b) device with 90 nm NiO_x. Reverse means scanning from open circuit voltage to short circuit current, and forward means scanning from short circuit current to open circuit voltage.

Figure 6 Comparison of device performance parameters obtained by different scanning direction. The subscript "r" represents scanning from open circuit voltage to short circuit current, and the subscript "f" represents scanning from short circuit current to open circuit voltage.

Figure 7 Air storage stability of the devices with different hole transport layers.

References

1. H. S. Jung and N.-G. Park, *Small*, 2015, **11**, 10-25.
2. S. D. Stranks, G. E. Eperon, G. Grancini, C. Menelaou, M. J. P. Alcocer, T. Leijtens, L. M. Herz, A. Petrozza and H. J. Snaith, *Science*, 2013, **342**, 341-344.
3. G. Xing, N. Mathews, S. Sun, S. S. Lim, Y. M. Lam, M. Graetzel, S. Mhaisalkar and T. C. Sum, *Science*, 2013, **342**, 344-347.
4. W. S. Yang, J. H. Noh, N. J. Jeon, Y. C. Kim, S. Ryu, J. Seo and S. I. Seok, *Science*, 2015, **348**, 1234-1237.
5. J. Burschka, N. Pellet, S.-J. Moon, R. Humphry-Baker, P. Gao, M. K. Nazeeruddin and M. Graetzel, *Nature*, 2013, **499**, 316-319.
6. M. M. Lee, J. Teuscher, T. Miyasaka, T. N. Murakami and H. J. Snaith, *Science*, 2012, **338**, 643-647.
7. J. M. Ball, M. M. Lee, A. Hey and H. J. Snaith, *Energy Environ. Sci.*, 2013, **6**, 1739-1743.
8. M. Liu, M. B. Johnston and H. J. Snaith, *Nature*, 2013, **501**, 395-398.
9. H. Zhou, Q. Chen, G. Li, S. Luo, T.-b. Song, H.-S. Duan, Z. Hong, J. You, Y. Liu and Y. Yang, *Science*, 2014, **345**, 542-546.
10. D. Liu and T. L. Kelly, *Nat. Photon.*, 2014, **8**, 133-138.
11. J. Liu, W. Yongzhen, C. Qin, X. Yang, T. Yasuda, A. Islam, K. Zhang, W. Peng, L. Han and W. Chen, *Energy Environ. Sci.*, 2014, **7**, 2963-2967.
12. Y. Shao, Z. Xiao, C. Bi, Y. Yuan and J. Huang, *Nat Commun*, 2014, **5**, 5784.
13. P.-W. Liang, C.-Y. Liao, C.-C. Chueh, F. Zuo, S. T. Williams, X.-K. Xin, J. Lin and A. K. Y. Jen, *Adv. Mater.*, 2014, **26**, 3748-3754.
14. Y. Chen, T. Chen and L. Dai, *Adv. Mater.*, 2015, **27**, 1053-1059.
15. K.-G. Lim, H.-B. Kim, J. Jeong, H. Kim, J. Y. Kim and T.-W. Lee, *Adv. Mater.*, 2014, **26**, 6461-6466.
16. J. H. Heo, D. H. Song, H. J. Han, S. Y. Kim, J. H. Kim, D. Kim, H. W. Shin, T. K. Ahn, C. Wolf, T.-W. Lee and S. H. Im, *Adv. Mater.*, 2015, **27**, 3424-3430.
17. J. H. Heo, H. J. Han, D. Kim, T. K. Ahn and S. H. Im, *Energy Environ. Sci.*, 2015, **8**, 1602-1608.

18. J. J. Jasieniak, J. Seifter, J. Jo, T. Mates and A. J. Heeger, *Adv. Funct. Mater.*, 2012, **22**, 2594-2605.

19. D.-D. Zhang, R. Wang, Y.-Y. Ma, H.-X. Wei, Q.-D. Ou, Q.-K. Wang, L. Zhou, S.-T. Lee, Y.-Q. Li and J.-X. Tang, *Org. Electron.*, 2014, **15**, 961-967.

20. E. L. Ratcliff, J. Meyer, K. X. Steirer, A. Garcia, J. J. Berry, D. S. Ginley, D. C. Olson, A. Kahn and N. R. Armstrong, *Chem. Mater.*, 2011, **23**, 4988-5000.

21. Z. Zhu, Y. Bai, T. Zhang, Z. Liu, X. Long, Z. Wei, Z. Wang, L. Zhang, J. Wang, F. Yan and S. Yang, *Angew. Chem. Int. Ed.*, 2014, **53**, 12571-12575.

22. K. C. Wang, J. Y. Jeng, P. S. Shen, Y. C. Chang, E. W. G. Diau, C. H. Tsai, T. Y. Chao, H. C. Hsu, P. Y. Lin, P. Chen, T. F. Guo and T. C. Wen, *Sci Rep*, 2014, **4**, 8.

23. K. C. Wang, P. S. Shen, M. H. Li, S. Chen, M. W. Lin, P. Chen and T. F. Guo, *ACS Appl. Mater. Interfaces*, 2014, **6**, 11851-11858.

24. X. Xu, Z. Liu, Z. Zuo, M. Zhang, Z. Zhao, Y. Shen, H. Zhou, Q. Chen, Y. Yang and M. Wang, *Nano Lett.*, 2015, **15**, 2402-2408.

25. J. H. Park, J. Seo, S. Park, S. S. Shin, Y. C. Kim, N. J. Jeon, H.-W. Shin, T. K. Ahn, J. H. Noh, S. C. Yoon, C. S. Hwang and S. I. Seok, *Adv. Mater.*, 2015, **27**, 4013-4019.

26. L. Hu, J. Peng, W. Wang, Z. Xia, J. Yuan, J. Lu, X. Huang, W. Ma, H. Song, W. Chen, Y.-B. Cheng and J. Tang, *ACS Photonics*, 2014, **1**, 547-553.

27. J.-Y. Jeng, K.-C. Chen, T.-Y. Chiang, P.-Y. Lin, T.-D. Tsai, Y.-C. Chang, T.-F. Guo, P. Chen, T.-C. Wen and Y.-J. Hsu, *Adv. Mater.*, 2014, **26**, 4107-4113.

28. Y. Bai, H. Yu, Z. L. Zhu, K. Jiang, T. Zhang, N. Zhao, S. H. Yang and H. Yan, *J. Mater. Chem. A*, 2015, **3**, 9098-9102.

29. J. H. Kim, P.-W. Liang, S. T. Williams, N. Cho, C.-C. Chueh, M. S. Glaz, D. S. Ginger and A. K. Y. Jen, *Adv. Mater.*, 2014, **27**, 695-701.

30. N. J. Jeon, J. H. Noh, Y. C. Kim, W. S. Yang, S. Ryu and S. I. Seok, *Nat Mater*, 2014, **13**, 897-903.

31. H.-S. Kim and N.-G. Park, *J. Phys. Chem. Lett.*, 2014, **5**, 2927-2934.

32. N. Tripathi, M. Yanagida, Y. Shirai, T. Masuda, L. Han and K. Miyano, *J. Mater. Chem. A*, 2015, **3**, 12081-12088.

33. H. Kim, K.-G. Lim and T.-W. Lee, *Energy Environ. Sci.*, 2015, DOI: 10.1039/C5EE02194D.

34. A. Kojima, K. Teshima, Y. Shirai and T. Miyasaka, *J. Am. Chem. Soc.*, 2009, **131**, 6050-6051.

35. S. Bai, Z. Wu, X. Wu, Y. Jin, N. Zhao, Z. Chen, Q. Mei, X. Wang, Z. Ye, T. Song, R. Liu, S.-t. Lee and B. Sun, *Nano Res.*, 2014, **7**, 1749-1758.

36. H. Wang, Y. Zhao, X. Li, C. Wu, X. Dong, Y. Ma, B. Zhang and G. Du, *Vacuum*, 2015, **119**, 77-80.

37. J. Xu, A. Buin, A. H. Ip, W. Li, O. Voznyy, R. Comin, M. Yuan, S. Jeon, Z. Ning, J. J. McDowell, P. Kanjanaboos, J.-P. Sun, X. Lan, L. N. Quan, D. H. Kim, I. G. Hill, P. Maksymovych and E. H. Sargent, *Nat. Commun.*, 2015, **6**, 7081.

38. E. L. Unger, E. T. Hoke, C. D. Bailie, W. H. Nguyen, A. R. Bowring, T. Heumueller, M. G. Christoforo and M. D. McGehee, *Energy Environ. Sci.*, 2014, **7**, 3690-3698.

39. A. Dualeh, T. Moehl, N. Tetreault, J. Teuscher, P. Gao, M. K. Nazeeruddin and M. Graetzel, *ACS nano*, 2014, **8**, 362-373.

40. H. J. Snaith, A. Abate, J. M. Ball, G. E. Eperon, T. Leijtens, N. K. Noel, S. D. Stranks, J. T.-W. Wang, K. Wojciechowski and W. Zhang, *J. Phys. Chem. Lett.*, 2014, **5**, 1511-1515.

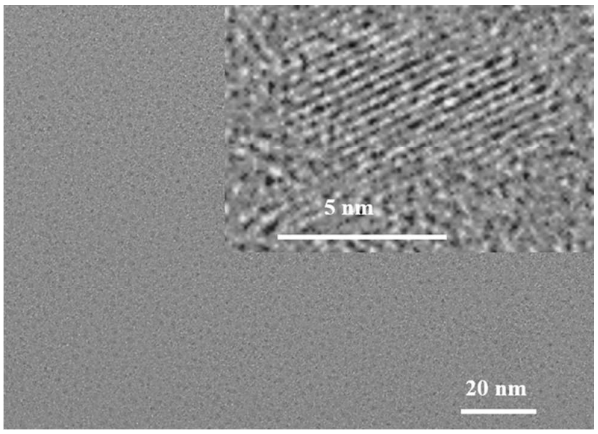

Figure 1

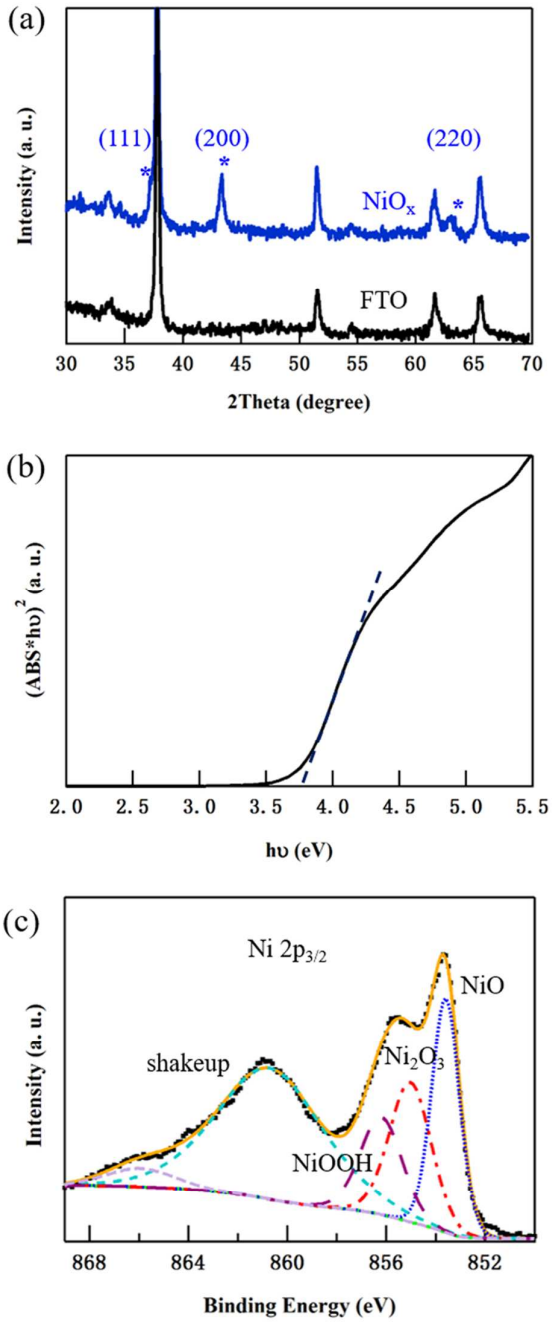
(a)
Intensity (a. u.)
(111)
(200)
(220)
NiOx
FTO
30 35 40 45 50 55 60 65 70
2Theta (degree)
(b)
(ABS*hυ)2 (a. u.)
2.0 2.5 3.0 3.5 4.0 4.5 5.0 5.5
hυ (eV)
(c)
Ni 2p3/2
NiO
Ni2O3
shakeup
NiOOH
Intensity (a. u.)
868 864 860 856 852
Binding Energy (eV)

Figure 2

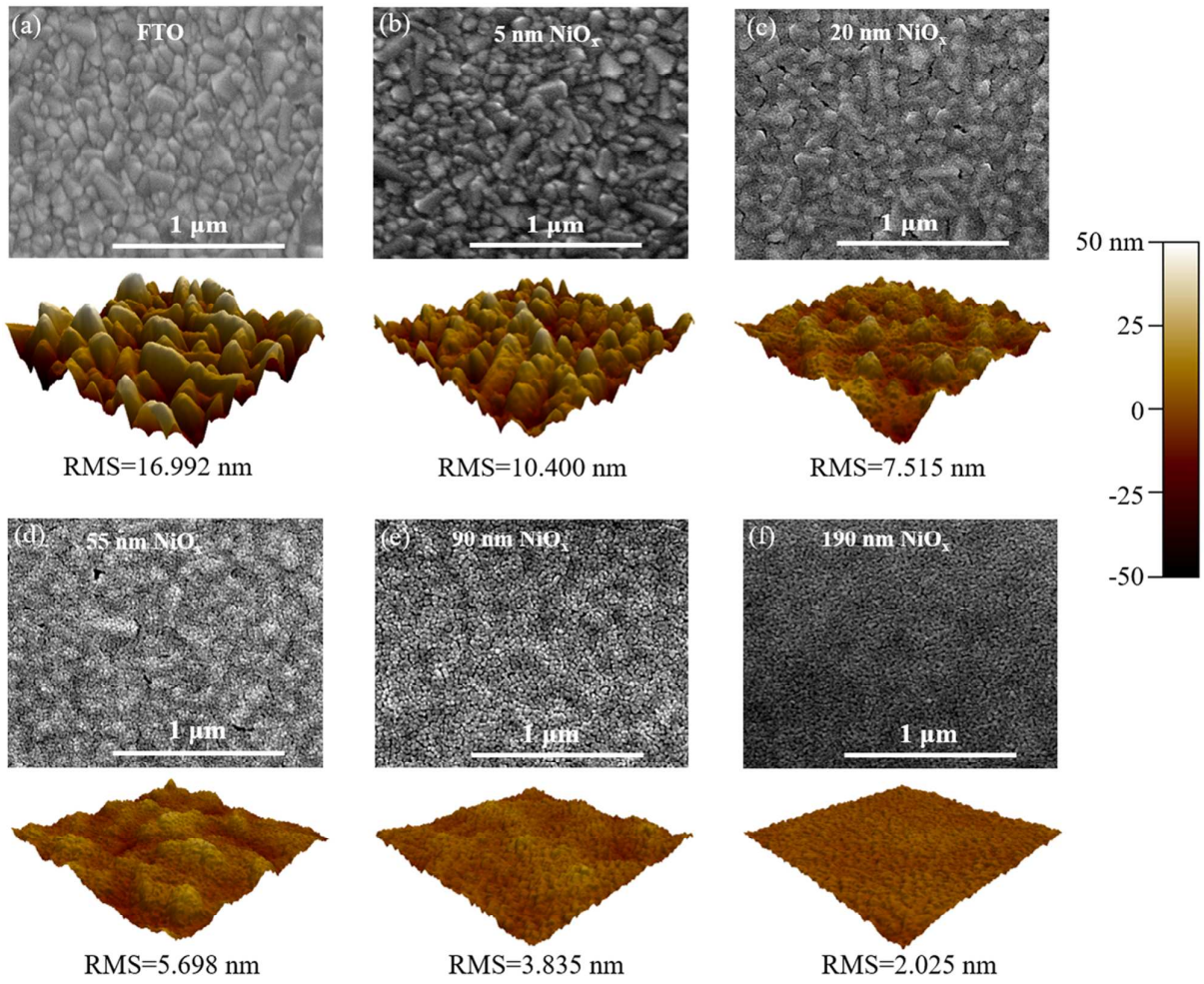
(a) FTO
1 µm
(b) 5 nm NiOx
1 µm
(c) 20 nm NiOx
1 µm
50 nm
25
0
-25
-50
RMS=16.992 nm
RMS=10.400 nm
RMS=7.515 nm
(d) 55 nm NiOx
1 µm
(e) 90 nm NiOx
1 µm
(f) 190 nm NiOx
1 µm
RMS=5.698 nm
RMS=3.835 nm
RMS=2.025 nm

Figure 3

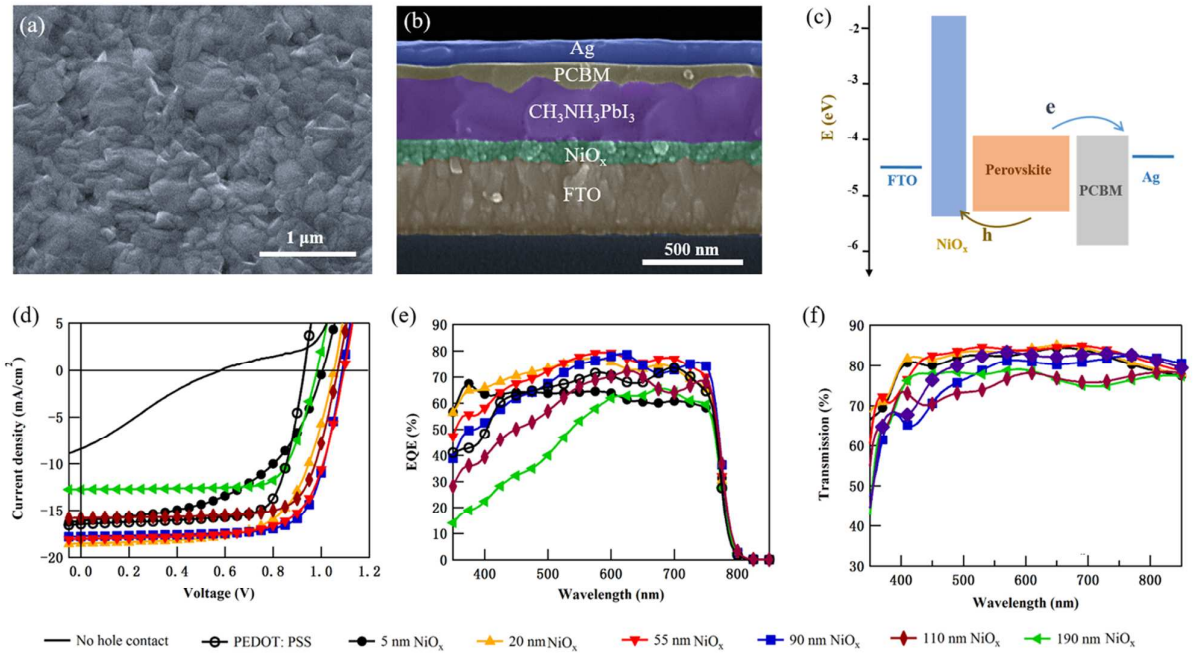
(a)
1 μm
(b)
Ag
PCBM
$CH_3NH_3PbI_3$
NiO_x
FTO
500 nm
(c)
E (eV)
FTO
NiO_x
Perovskite
PCBM
Ag
e
h
(d)
Current density (mA/cm^2)
Voltage (V)
(e)
EQE (%)
Wavelength (nm)
(f)
Transmission (%)
Wavelength (nm)
No hole contact
PEDOT: PSS
5 nm NiO_x
20 nm NiO_x
55 nm NiO_x
90 nm NiO_x
110 nm NiO_x
190 nm NiO_x

Figure 4

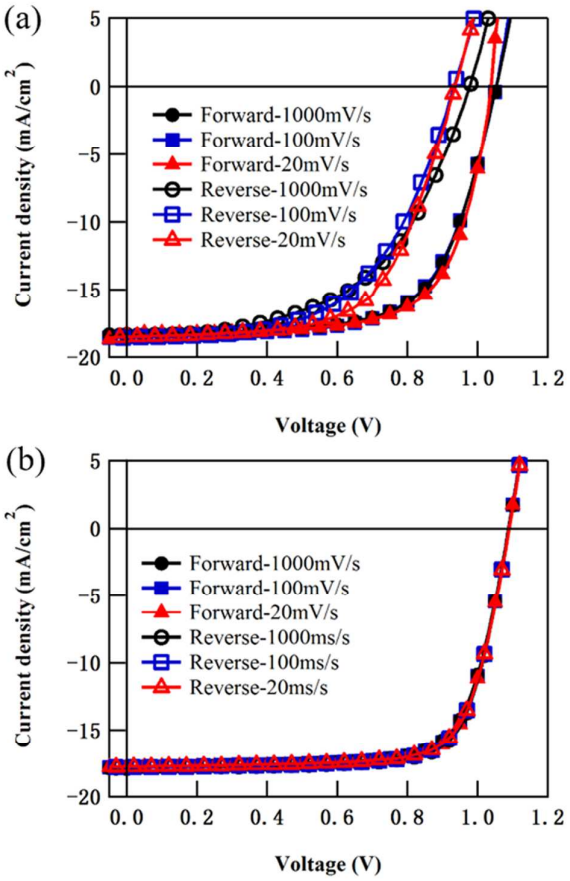
(a)
Current density (mA/cm^2)
5
0
−5
−10
−15
−20
0.0
0.2
0.4
0.6
0.8
1.0
1.2
Voltage (V)
Forward-1000mV/s
Forward-100mV/s
Forward-20mV/s
Reverse-1000mV/s
Reverse-100mV/s
Reverse-20mV/s
(b)
Current density (mA/cm^2)
Voltage (V)
Forward-1000mV/s
Forward-100mV/s
Forward-20mV/s
Reverse-1000ms/s
Reverse-100ms/s
Reverse-20ms/s

Figure 5

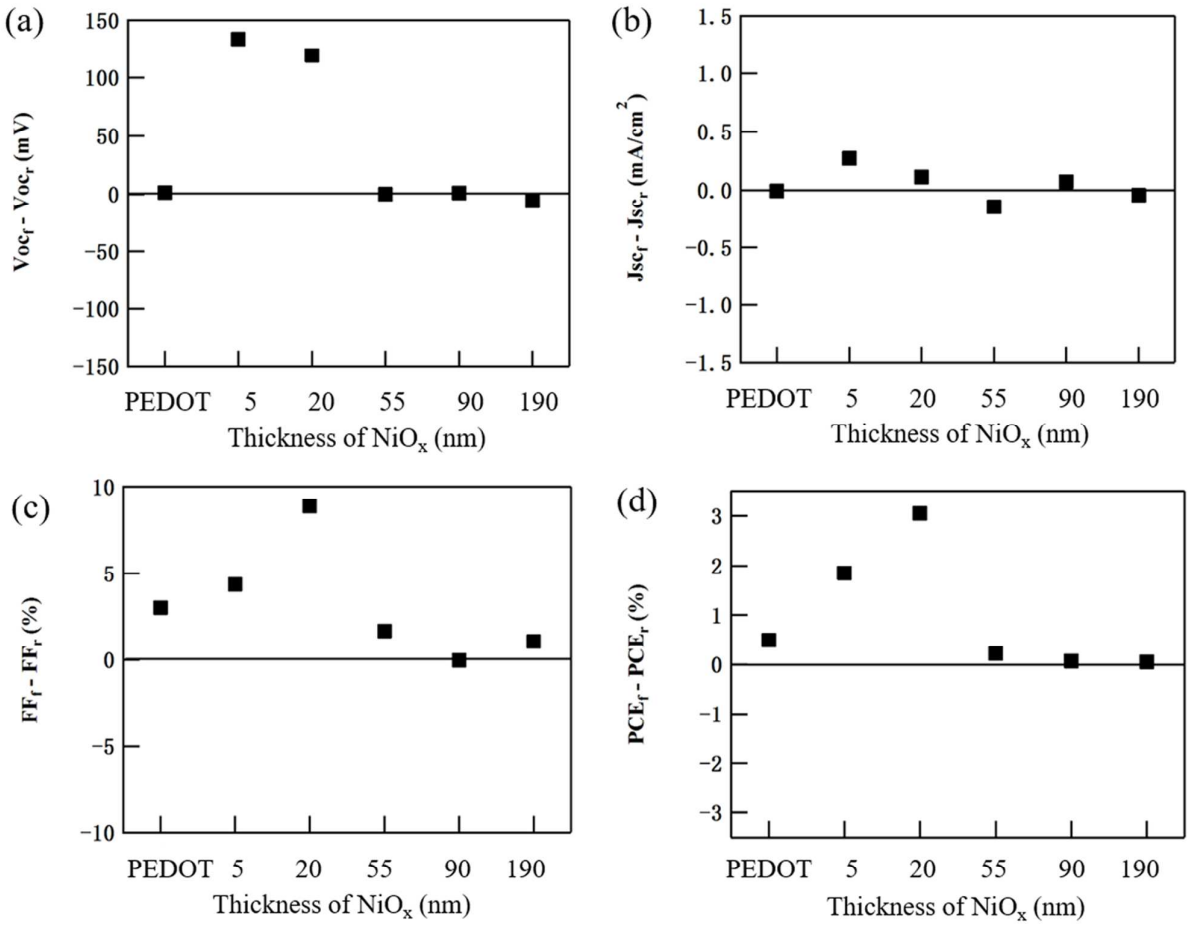
(a)
150
100
50
0
−50
−100
−150
Voc_r - Voc_r (mV)
PEDOT 5 20 55 90 190
Thickness of NiO_x (nm)
(b)
1.5
1.0
0.5
0.0
−0.5
−1.0
−1.5
Jsc_r - Jsc_r (mA/cm^2)
PEDOT 5 20 55 90 190
Thickness of NiO_x (nm)
(c)
10
5
0
−5
−10
FF_r - FF_r (%)
PEDOT 5 20 55 90 190
Thickness of NiO_x (nm)
(d)
3
2
1
0
−1
−2
−3
PCE_r - PCE_r (%)
PEDOT 5 20 55 90 190
Thickness of NiO_x (nm)

Figure 6

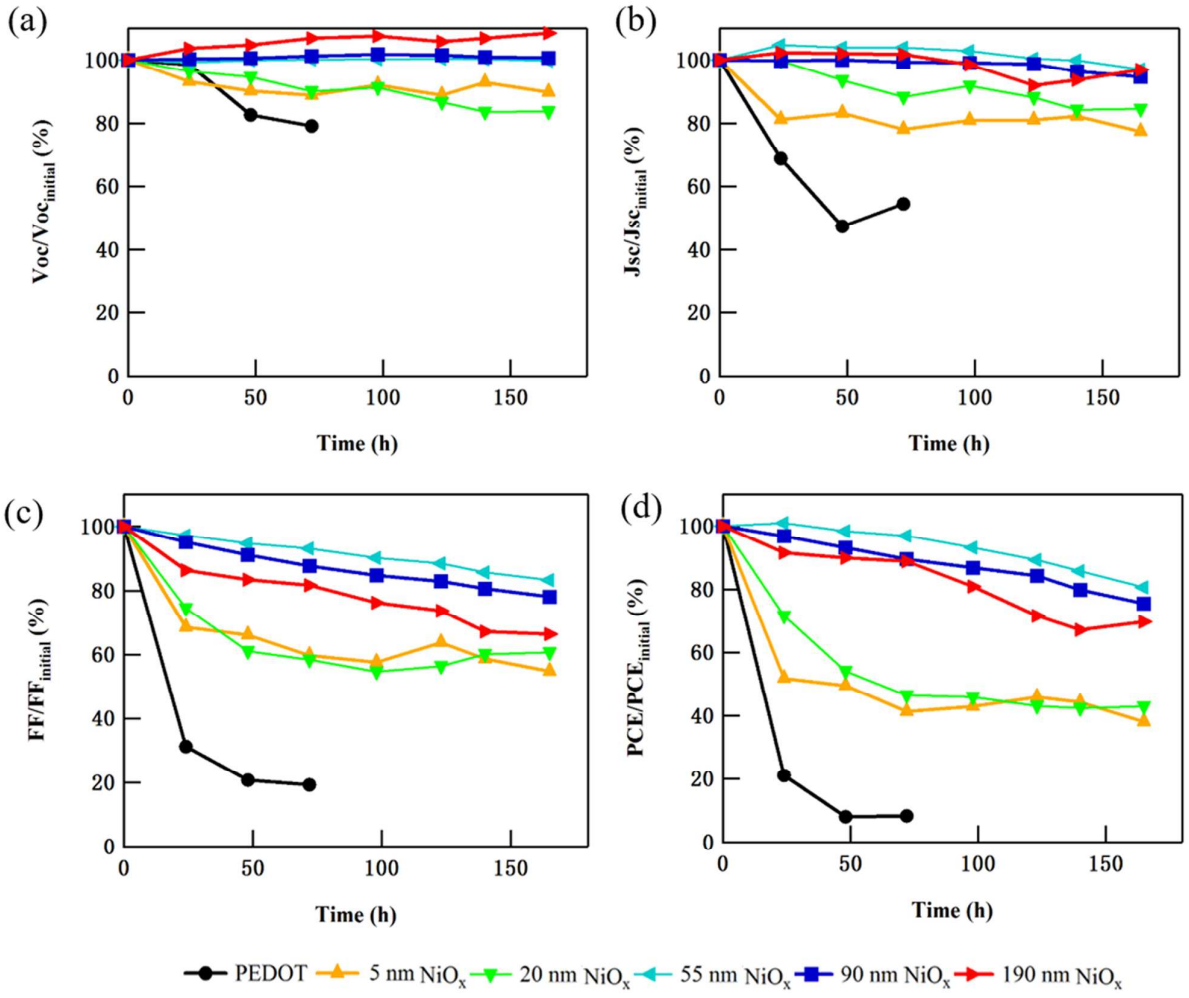
(a)
Voc/Voc$_{initial}$ (%)
Time (h)
(b)
Jsc/Jsc$_{initial}$ (%)
Time (h)
(c)
FF/FF$_{initial}$ (%)
Time (h)
(d)
PCE/PCE$_{initial}$ (%)
Time (h)
PEDOT
5 nm NiO$_x$
20 nm NiO$_x$
55 nm NiO$_x$
90 nm NiO$_x$
190 nm NiO$_x$

Figure 7

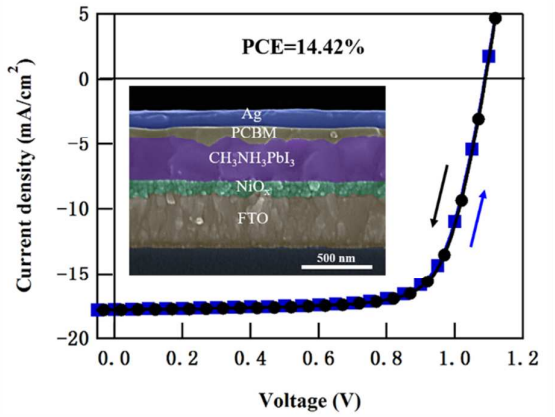

Solution-derived NiO_x film was successfully employed to work as the hole selective contact for high efficiency inverted planar heterojunction perovskite with negligible hysteresis.